Resolving breakup in flash atomization conditions using DNS

D. Loureiro[1⋆], J. Reutzsch[2], A. Kronenburg[1], B. Weigand[2], K. Vogiatzaki[3]

[1]Institute for Combustion Technology, University of Stuttgart, Germany,

[2]Institute of Aerospace Thermodynamics, University of Stuttgart, Germany,

[3]Advanced Engineering Centre, University of Brighton, UK.

⋆Corresponding author. daniel.dias-loureiro@itv.uni-stuttgart.de

Keywords: Flash boiling atomization, Cryogenic fluid, Phase change, Interface capturing DNS

Abstract

Flash boiling can occur in rocket thrusters operating in the vacuum of space when cryogenic propellants are injected into the reaction chamber that is initially at low pressure. The dynamics of this process will determine the spray breakup that will then drastically affect the mixing of fuel and oxidizer, the reliability of the ignition and the subsequent combustion process. A multiphase solver with interface capturing is used to perform direct numerical simulations (DNS) of the primary breakup of the liquid oxygen jet that is driven by homogeneous nucleation, growth, coalescence and bursting of vapour bubbles in the superheated liquid. Considering the main breakup patterns and droplet formation mechanisms for a range of conditions, we evaluate the effectiveness of the volume of fluid (VoF) with continuum surface stress (CSS) method to capture the breakup of thin lamellae formed at high Weber numbers. A grid refinement study shows convergence of the mass averaged droplet size towards a droplet diameter. The order of magnitude of the resulting diameter can be estimated based on the thermodynamic conditions.

1 Introduction

Flash boiling can occur in rocket thrusters operating in the vacuum of space when the liquid propellants are injected into the reaction chamber that is initially at very low pressure. The dynamics of this process will determine the spray break-up that will then drastically affect the mixing of fuel and oxidizer, the reliability of the ignition and the subsequent combustion process. This becomes particularly relevant in upper stage engines and orbital maneuvering systems where multiple precise ignitions are to be performed. To simplify the spacecraft design and facilitate ground handling, there is a trend to replace toxic mono-propelants like hydrazine with cryogenic bi-propellant alternatives such as LH2-LOx or LCH4-LOx, as well as eliminating the use of igniter fluids with the use of focused lasers (Manfletti (2014); Hurlbert et al. (1998)). Particularly when coaxial injectors are used, one key parameter is the spreading angle of the central jet (LOx) as it will influence the location of the mixing layer. This is highly influenced by the occurrence of flash boiling along with other characteristics of the spray.

The fundamental physics of flash atomization are introduced in the work of Sher et al. (2008). Flashing occurs when a liquid experiences a rapid drop in pressure to a value below its saturation condition. In this meta-stable superheated state, microscopic vapour bubbles spontaneously nucleate within the continuous liquid phase (homogeneous nucleation). This is followed by rapid expansion that leads to the jet disintegration and extremely fast evaporation.

In this work we focus on the microscopic processes leading to the primary break-up of a liquid oxygen jet in fully flashing conditions (high levels of superheat) and without the influence of aerodynamic breakup. Direct Numerical simulations (DNS) are performed on a small domain, representative of the conditions that would be found near the exit of the injector nozzle. With fully resolved bubbles and the introduction of phase change at the interface, we simulate the growth, deformation and coalescence of multiple bubbles, leading to the formation of ligaments and liquid films that breakup and burst into small droplets that constitute the spray.

An overview of the dynamics of bubble growth can be found in various works including Sher et al. (2008) and Prosperetti (2017). With the assumption of spherical symmetry, the various stages of growth are generally modeled using the Raleigh-Plesset equation coupled with heat transfer at the bubble interface due to the latent heat of evaporation. This can be done using approximate analytical solutions, e.g. Scriven (1959), or solved exactly using numerical methods (Lee and Merte (1996)). Although the model of Scriven (1959) is widely used in DNS with phase change, it is shown by Bardia and F. Trujillo (2018) that it is only valid in the later stages of bubble growth. As detailed in Loureiro et al. (2018), the numerical approach of Lee and Merte (1996) is used as a reference throughout this work and will be referred to as R-P solution.

Based on dimensional analysis for general types of breakup, a model for droplet size estimation was proposed by Hinze (1955). Estimation of droplet sizes resulting from flash atomization were proposed by Sher and Elata (1977), with the assumption that under very high nucleation rates, the bub-

bles would form a close-packing cubic array and merge immediately. Later, Razzaghi (1989) used an analytical model based on Rayleigh-Taylor instability and Monte-Carlo computational methods to estimate the droplet sizes resulting from the growth of a single bubble inside a droplet that is already detached from the bulk of the liquid. More recently, Zeng and Lee (2001) combined this approach with a conventional aerodynamic breakup model. For all these approaches there are severe assumptions and simplifications regarding the microscopic structure of the problem, while studies involving the interaction of an arbitrary number of bubbles in irregular distributions have not been found in the literature. In this work, no assumptions are necessary regarding bubble distribution or the type of interface instability behind the breakup. Nonetheless, regular arrays of equally spaced bubbles are used here, simply for the purpose of repeatability, systematic comparison of different setup conditions and for the initial validation of the method.

Simulations of atomization processes using high fidelity capturing of the liquid vapour interface have recently become possible thanks to modern computational resources. Early DNS of liquid jet breakup include Desjardins et al. (2008), Lebas et al. (2009) and Shinjo and Umemura (2010), where the formation of the small scale liquid structures and their breakup into small droplets is analysed. More recently Zhu et al. (2013) and Ertl et al. (2018) have used similar setups for the breakup of Non-Newtonian fluids using structured meshes, using the same numerical tools as used in this work. Chen et al. (2013) simulated the breakup of impinging jets using adaptive mesh refinement (AMR).

These are generally referred as DNS in the sense that the smallest Kolmogorov length scale is resolved, at least in the liquid phase. However, for primary atomization DNS, the smallest possible liquid structure needs to be resolved. As pointed out by Gorokhovski and Herrmann (2008), every DNS of liquid breakup implies topological changes that cannot be resolved by DNS within the continuum assumption of the Navier-Stokes equations. However, in interface capturing methods, the topological change is automatically introduced once the distance between two interfaces can no longer be resolved by the mesh. This means that the size of the smallest liquid structure and the exact moment of the breakup are related with the resolution and methods used. It is generally observed in these works that the number of artificially generated droplets is highly dependent on the mesh resolution, even when AMR is used, particularly for higher Weber and Reynolds numbers. For the numerical methods used in this work, this problem has been analysed by Liu and Bothe (2016). However, in most situations, it is possible to verify that these droplets represent a very small fraction of the total liquid mass and have very little effect in the global spray characteristics.

Following the observations in Loureiro et al. (2018) we now focus on the breakup of thin lamellae. These are formed in between bubbles. They deform and resist merging, until they burst into a very large number of artificial droplets once the resolution threshold is reached. An analysis on stability of thin films (Ruckenstein and Jain (1974)) implies the action of inter-molecular forces which are not modeled here. However, it is expected that – once the initial (artificially induced) puncture of the lamella has occurred – the lamella breakup process can be fully resolved as it is driven by the propagation of capillary waves.

In this context, a resolution criterion for DNS is sought such that the artificial droplets related to the mesh size are insignificant in terms of mass and area compared to the real droplet size distribution, and a resolution criterion could thus be established.

2 Numerical Methods

In flashing of cryogenic liquids, the low temperatures and the near vacuum pressure ensures sub-critical conditions, where the gas and liquid phases have a large density ratio and a well defined interface for each individual bubble. At this scale the interface velocities are relatively low and these conditions are well suited for DNS using a multi-phase incompressible solver with high fidelity interface capturing.

The DNS is performed using the in-house code Free-Surface 3D – FS3D (Eisenschmidt et al. (2016)). The code uses a finite volume method to discretize the incompressible Navier-Stokes equations, while capturing a fully resolved liquid-vapour interface with phase change and surface tension, using the Volume of Fluid (VoF) method with PLIC reconstruction.

In the VoF method (Hirt and Nichols (1981)) an additional variable is transported representing the volume fraction of liquid in the cell, f. Hence, $f = 1$ in the liquid phase, $f = 0$ in the gas phase and $0 < f < 1$ in the cells containing the interface. Following Schlottke and Weigand (2008), the discretized transport equation with evaporation can be written as

$$\frac{\partial f}{\partial t} + \nabla \cdot (f \mathbf{u}_\Gamma) = \frac{\dot{m}'''}{\rho_\ell}, \tag{1}$$

where $\mathbf{u}_\Gamma$ is the interface velocity and $\dot{m}'''$ is the liquid evaporation rate at the interface.

The PLIC (piecewise linear interface calculation) scheme (Rider and Kothe (1998)) consists of determining an interface plane for each finite volume cell, the normal vector of which is determined from the gradient of the VoF field, $\hat{\mathbf{n}}_\Gamma = -\frac{\nabla f}{\|\nabla f\|}$, and the exact position within the cell is determined by matching the volume bound by the plane with the volume fraction f.

Volume averaged fluid properties are used – density $\rho = \rho_\ell f + \rho_v (1 - f)$ and viscosity $\mu = \mu_\ell f + \mu_v (1 - f)$ – in order to solve the Navier-Stokes equations using a single continuous velocity, $\mathbf{u}$, and pressure, p, field, viz.

$$\frac{\partial}{\partial t}(\rho \mathbf{u}) + \nabla \cdot [\rho \mathbf{u}\mathbf{u}] = \nabla \cdot \mu \left[\nabla \mathbf{u} + \nabla (\mathbf{u})^T\right] - \nabla p + \mathbf{f}_\sigma. \tag{2}$$

Here, buoyancy forces have been neglected and the only additional force considered is surface tension, $\mathbf{f}_\sigma$.

The surface tension term $\mathbf{f}_\sigma$ is introduced as a volumetric force acting only in the vicinity of the interface, using the continuum surface stress (CSS) model of Lafaurie et al. (1994).

This model is selected for its flexibility and low resolution requirements when modeling bubble coalescence, liquid

breakup and droplet collisions. However, as shown by Liu and Bothe (2016), it may lead to unphysical interaction between the two interfaces of a thin lamella, if their distance is smaller than 4 computational cells. This corresponds to the width of the stencil around the interface used to calculate $\mathbf{f}_\sigma$.

With the assumption of incompressibility, the pressure field p is defined implicitly by the pressure Poisson Equation

$$\nabla \cdot \left[\frac{1}{\rho(f)} \nabla p \right] = \frac{\nabla \cdot \mathbf{u}}{\Delta t} \tag{3}$$

where the continuity equation is introduced through the velocity divergence term $\nabla \cdot \mathbf{u}$ and solved using an efficient multi-grid solver (Rieber (2004)).

Due to phase change with large density ratio, there is a jump condition in the continuity equation at the interface. This means $\nabla \cdot \mathbf{u} = 0$ except in cells with $0 < f < 1$, where it is determined as a function of the evaporation rate $\dot{m}'''$. This naturally introduces the jump condition in the momentum conservation equation through the pressure field p. As detailed by Schlottke and Weigand (2008), mass conservation is ensured in the volume weighted velocity field $\mathbf{u}$, through a correction of the divergence term, $\nabla \cdot \mathbf{u}^\star$, which is based on the individual velocities of the vapour and liquid phases, $\mathbf{u}_v$ and $\mathbf{u}_\Gamma$, under consideration of the reconstructed interface geometry, evaporation rate and fluid densities.

In the current approach no additional equations are solved and the evaporation rate is introduced as an external parameter. Assuming ρ_v to be approximately constant, we define

$$\dot{m}''' = a_\Gamma \dot{m}'' = a_\Gamma \rho_v \dot{R} \tag{4}$$

where $\dot{m}''$ is the evaporation mass flux and a_Γ is the interface density (interface area per unit of volume). Here, we replace the unknown $\dot{m}''$ by growth rate of a spherical bubble, $\dot{R}$, which acts as an imposed interface velocity.

3 Setup Method

As previously detailed in Loureiro et al. (2018), the simulation domain represents a small volume of continuous liquid near the exit of the injector nozzle or within a large droplet within the spray as depicted in Fig. 1.

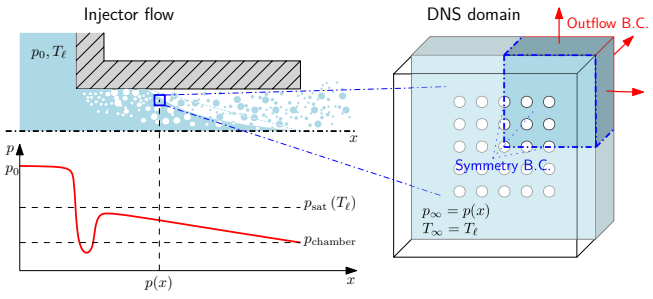

Figure 1: Schematic of flashing flow in the injector and simulation domain.

The DNS domain is populated with a regular array of uniformly spaced bubbles that grow and coalesce, leaving behind droplets resulting from the breakup of liquid ligaments, lamellae and other liquid structures formed by the interstitial liquid. The liquid is initially static (relative to the jet velocity), has no interaction with the injector walls (no shear layer) and is free to expand through the use of continuity boundary conditions (outflow). Large buffer zones of pure liquid are used to prevent the interaction of the liquid vapour interface with the boundaries. Finally, symmetry conditions are used to reduce the computational cost.

The reference liquid temperature and ambient pressure conditions for the DNS, T_∞ and p_∞, correspond to local conditions that could be found in the relevant jet section. These are the injection temperature T_ℓ and the local pressure $p(x)$. They are treated as free parameters.

The initial spacing between the bubbles is assumed to be uniform and should be related to the nucleation rate J and the mass flow rate. Since here a mass flow rate is not defined, such dependence is avoided and the bubble spacing is treated as a free geometric parameter. As such, we define the parameter R_f as the final bubble radius at which the bubbles are expected to touch and start merging. Considering p_∞ and T_∞, we use the critical radius as a reference value and normalize R_f, $R_f^* = R_f / R_{\text{crit}}$. The normalized quantity represents a growth factor since nucleation.

The critical radius corresponds to the minimum bubble radius at which the surface tension is in equilibrium with the vapour pressure, $p_v = p_{\text{sat}}(T_\infty)$, and is given by

$$R_{\text{crit}} = \frac{2\sigma}{p_{\text{sat}}(T_\infty) - p_\infty}, \tag{5}$$

where σ is the surface tension coefficient at T_∞.

Finally, we estimate the initial bubble distance that will lead to coalescence given the final bubble radius R_f with the equation

$$D_0 = R_f \sqrt[3]{8 - \frac{4\pi}{3}\left(1 - \frac{\rho_v}{\rho_\ell}\right)\left(1 - \frac{R_i^3}{R_f^3}\right)}. \tag{6}$$

This equation results from conservation of mass in the control volume $(2R_f)^3$.

The geometric parameter R_f or R_f^* can therefore be correlated to a nucleation rate or bubble number density that would be expected for a particular injection condition or, in the context of an LES-SGS model, to the local (current) value of the transported variables such as vapour volume fraction and surface area.

With the parameters p_∞ and T_∞, we use the R-P solution for single bubble growth to determine the growth rate, $\dot{R}$, vapour density ρ_v, surface tension coefficient, σ, and vapour viscosity, μ_v, as functions of R_f or R_f^*.

This approach calibrates the parameters that account for the influence of interface cooling and vapour compressibility at the target bubble size and implicitly compensates for the constant properties assumption that holds throughout the DNS simulation. This is particularly relevant for the volume of vapour generated through Eq. 4, which determines the liquid velocity and the breakup characteristics, together with surface tension and viscous forces.

For cases where extreme variations of $\dot{R}$ are expected (early stages of bubble growth), the growth rate can be tabulated as a function of the bubble size and adjusted in real-time, as detailed in Loureiro et al. (2018). However, for

the results presented here, $\dot{R}$ is assumed constant, which is a good approximation (order of 10%) for bubbles in the transition to the diffusion controlled stage of growth.

The liquid properties ρ_ℓ and μ_ℓ are obtained directly as function of p_∞ and T_∞, using the equation of state library CoolProp (Bell et al. (2014)).

Using the interface velocity, $\dot{R}$, and the final bubble diameter, $2R_f$, as reference velocity and length scales, we define the Weber and Ohnesorge number as

$$\mathrm{We}_b = \frac{\rho_\ell \dot{R}^2 2R_f}{\sigma}, \tag{7}$$

and

$$\mathrm{Oh}_b = \frac{\mu_\ell}{\sqrt{\rho_\ell \sigma 2R_f}}. \tag{8}$$

Here, the subscript b denotes that these numbers relate to the characteristics of the bubbles and not to the injector flow.

4 Study Description

In this study, we focus on two cases with $T_\infty = 120\,\mathrm{K}$ (case A) and $T_\infty = 80\,\mathrm{K}$ (case B), both at pressures of $p_\infty = 1000\,\mathrm{Pa}$. This corresponds to the range of injection temperatures and the minimum vacuum pressure for corresponding experiments carried out at a test bench for cryogenic injection that is maintained in the Institute of Space Propulsion at DLR Lampoldshausen.

These two cases are selected as earlier studies showed that Oh_b is generally below 0.1 for the entire range of conditions examined at DLR and that the type of break-up primarily depends on We_b. It is apparent that We_b depends on R_f and we therefore set for both cases $R_f^* = 50$, for which $\mathrm{We}_b > 20$ and the formation of thin lamellae is expected (Loureiro et al. (2018)).

For each case the simulation domain represents a regular array of $3 \times 3 \times 3$ bubbles. Considering the symmetry boundary conditions, this means that 3 bubble contact points are fully resolved, resulting in one lamella parallel to each Cartesian plane. The initial setup and final lamellae formation will be shown in Fig. 2 in the following section.

Although the same type of breakup patterns are expected for these Weber numbers, the difference in T_∞ implies a 2 order of magnitude scaling factor in terms of length scales.

A third case, C, with $R_f^* = 175$ was chosen to match the same We_b as case B, but at the higher temperature $T_\infty = 120\,\mathrm{K}$. This acts as a plausibility check to verify the negligible effects of Oh_b, the thermodynamic conditions, and length scale. As expected case B and C generate qualitatively similar sprays and show the same trend regarding the mesh refinement, except for a scaling factor of the spatial dimensions. Therefore, the results for case C are not shown.

A list of set up parameters and relevant characteristics is defined in Tab. 1. The physical conditions for flash atomization are typically characterised by p_∞, T_∞, the superheat and the pressure ratio. The level of superheat is defined as

$$\Delta T = T_\infty - T_{\mathrm{sat}}(p_\infty), \tag{9}$$

or in terms of pressure, through the pressure ratio as

$$R_p = \frac{p_{\mathrm{sat}}(T_\infty)}{p_\infty}, \tag{10}$$

where the subscript, "sat" denotes saturation conditions. The table also contains the levels of mesh refinement tested, where Δx denotes the cell length, with $\Delta x = \Delta y = \Delta z$.

Table 1: Simulation parameters and grid refinement levels

Case	A	B	C (Control)
T_∞	$120\,\mathrm{K}$	$80\,\mathrm{K}$	$120\,\mathrm{K}$
p_∞	$1000\,\mathrm{Pa}$	$1000\,\mathrm{Pa}$	$1000\,\mathrm{Pa}$
ΔT	$58.71\,\mathrm{K}$	$18.71\,\mathrm{K}$	$58.71\,\mathrm{K}$
R_p	1022	30.12	1022
R_f^*	50	50	175
R_{crit}	$0.012\,\mu\mathrm{m}$	$1.01\,\mu\mathrm{m}$	$0.012\,\mu\mathrm{m}$
We_b	33	80	80
Oh_b	2.9×10^{-2}	5.66×10^{-3}	1.5×10^{-2}
D_{ref}	$0.285\,\mu\mathrm{m}$	$10.77\,\mu\mathrm{m}$	$0.418\,\mu\mathrm{m}$
128^3 grid: $\Delta x = R_f/14$	$4.2 \times 10^{-8}\,\mathrm{m}$	$3.8 \times 10^{-6}\,\mathrm{m}$	$1.5 \times 10^{-7}\,\mathrm{m}$
256^3 grid: $\Delta x = R_f/28$	$2.1 \times 10^{-8}\,\mathrm{m}$	$1.9 \times 10^{-6}\,\mathrm{m}$	$7.4 \times 10^{-1}\,\mathrm{m}$
512^3 grid: $\Delta x = R_f/57$	$1.1 \times 10^{-8}\,\mathrm{m}$	$9.5 \times 10^{-7}\,\mathrm{m}$	$3.7 \times 10^{-8}\,\mathrm{m}$
1024^3 grid: $\Delta x = R_f/114$	$5.3 \times 10^{-9}\,\mathrm{m}$	–	–

As a reference for the expected droplet size, a lower bound for the droplet diameter, D_{ref}, can be estimated in terms of energy conservation. Here, we equate the droplet's volumetric surface energy, $4\sigma/D_{\mathrm{ref}}$, with the available kinetic energy in the liquid, $\rho_\ell \dot{R}^2/2$, as

$$D_{\mathrm{ref}} = \frac{8\sigma}{\rho_\ell \dot{R}^2}. \tag{11}$$

This estimator shall be understood as an order of magnitude estimate for the prediction of mesh resolution requirements. The real minimum droplet diameter may deviate from this estimate since $\dot{R}$ considers a local interface velocity of a single bubble only and bubble interactions and convective effects may alter the local (relevant) kinetic energy that leads to a lamella breakup.

5 Results

The mechanics of the breakup process are visualised in Fig. 2. The bubbles grow and merge at the first point of contact (see Fig. 2.b as indicated by the "punctured" bubbles). The fluid between the bubble does not fully retract immediately, but relatively flat thin liquid layers persist. At the puncture point, a rim is formed, which starts to retract radially. The fluid velocity, shown by the colour scale shows that the rim retraction propagates rather quickly in comparison to the growth rate, and more droplets seem to be generated when this velocity is at its peak (Figs. 2.c and .d). For this case, the number of droplets generated is rather low and and most of the droplets are well resolved.

In Fig. 3, Case B is shown at it's final stage of breakup, for different refinement levels. Here, the colour scale depicts the local radius, which helps to identify the presence of very

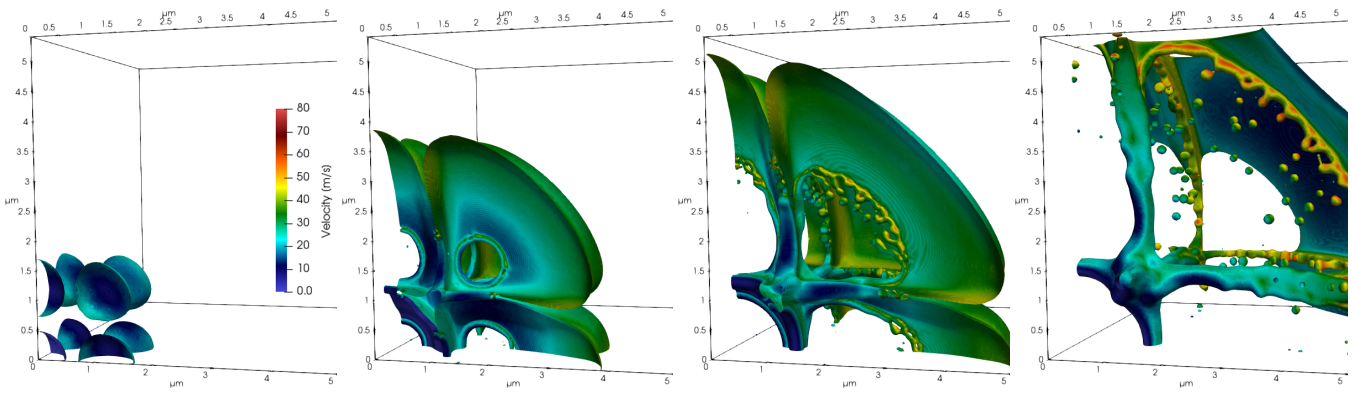

(a) $t = 0.022\,\mu s$ **(b)** $t = 0.067\,\mu s$ **(c)** $t = 0.089\,\mu s$ **(d)** $t = 0.126\,\mu s$

Figure 2: Sequence of time steps of bubble growth and lamella rupture for Case A with 512^3 grid. the bubble interface is rendered by the $f = 0.01$ iso-surface and coloured according to the velocity magnitude.

small satellite droplets generated artificially. With increased resolution, the droplets generated seem to be well resolved and stable, but their number and size still changes between the 256^3 grid and 512^3 grid. It is expected, however, that as in case A, differences to a 1024^3 grid case would be small as will be subject of future work.

5.1 Statistical Analysis

To verify convergence of the results with mesh refinement, the statistics of droplet sizes are analysed.

The first step in the analysis requires the classification of the liquid structures, droplets and ligaments, that constitute the the spray. A domain search is performed to find the limits of continuous regions with $f > 0.01$ that correspond to a liquid structure or droplet. For each identified zone, i, the liquid volume is calculated by

$$V_i = \sum_{k=1}^{n_k} f_k (\Delta x_k)^3, \tag{12}$$

where n_k is the number of cells in the droplet and $(\Delta x_k)^3$ is the cell volume. The equivalent spherical diameter D_i is then calculated as

$$D_i = \sqrt[3]{\frac{6}{\pi} V_i}. \tag{13}$$

As shown in figures 2 and 3, at any given instant the domain contains a combination of large ligaments still in the process of breaking up, medium sized stable droplets, small artificial or satellite droplets and isolated cells with $f < 1$ which cannot be resolved. To achieve robust result, only the stable droplets (both medium size and artificial/satellite) are included in the statistical sample. This is achieved through the following steps:

1. for each droplet the inertia tensor $[I]$ and principal moments of inertia, I_{xx}, I_{yy} and I_{zz}, are calculated by eigendecomposition;

2. the equivalent ellipsoid with the semi-axes a, b, c is determined by

$$\begin{aligned} a^2 &= \frac{5\left(-I_{xx} + I_{yy} + I_{zz}\right)}{2V_i}, \\ b^2 &= \frac{5\left(I_{xx} - I_{yy} + I_{zz}\right)}{2V_i}, \\ c^2 &= \frac{5\left(I_{xx} + I_{yy} - I_{zz}\right)}{2V_i} \end{aligned} \tag{14}$$

and its volume calculated as

$$V_i^e = \frac{4}{3}\pi abc; \tag{15}$$

3. a filter is applied to select only the droplets for which the ellipsoidal volume V_i^e matches the original f-based volume V_i within an adjusted tolerance of 20%, viz.

$$j \in \left\{ i : \frac{V_i^e}{V_i} - 1 < 20\% \right\}. \tag{16}$$

This filter implies that the fully atomized (stable) droplets are approximately spherical or ellipsoidal (possibly oscillating) and excludes large ligaments or any residual droplets that do not have enough volume to be resolved.

Finally, the representative diameters of the spray are defined using the filtered set of droplets. D_{10} corresponds to the arithmetic mean

$$D_{10} = \sum_{i \in j}^{N_j} D_i \Big/ N_j, \tag{17}$$

D_{32} is the Sauter mean diameter (area-weighted mean)

$$D_{32} = \sum_{i \in j}^{N_j} D_i^3 \Big/ \sum_{i \in j}^{N_j} D_i^2, \tag{18}$$

and D_{43} is De Brouckere mean diameter

$$D_{43} = \sum_{i \in j}^{N_j} D_i^4 \Big/ \sum_{i \in j}^{N_j} D_i^3 \tag{19}$$

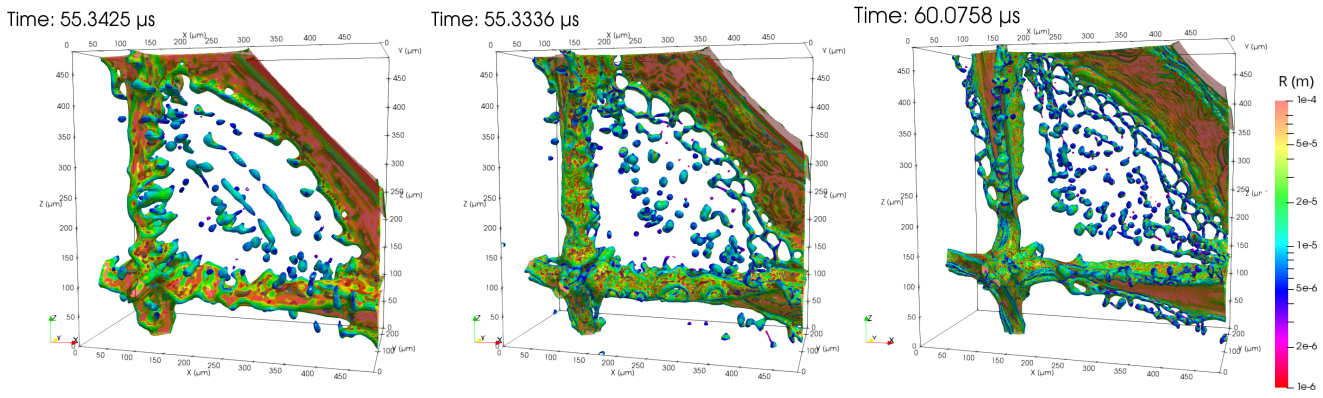

(a) 128^3 **(b)** 256^3 **(c)** 512^3

Figure 3: Refinement levels Case B. breakup patterns represented by Iso-surface VoF$= 0.5$ and coloured by local radius.

which corresponds to the mass-weighted mean of the spray. This filtering process ensures the analysis' independence of the specific time during the break-up process when statistics are sampled.

The dependency of the mean droplet diameters, D_{10}, D_{32} and D_{43} on the mesh refinement is shown in Fig. 4. Both cases demonstrate convergence of the D_{32} and D_{43} mean diameters, but final conclusions may require the additional data from a final simulation of case B with 1024^3 grid nodes.

The convergence of the D_{32} and D_{43} means that the diameter of the droplets with the largest area and volume (or mass), respectively, does not not vary significantly with resolution beyond the 512^3 grid. This provides a resolution criterion of $dx = R_f/57$. The larger sensitivity of D_{10} is due to the generation of a large number of artificial droplets. This is expected as has been documented in the archival literature.

The normalized droplet size distributions shown in Fig. 7 provide a more quantitative measure and demonstrate more clearly the dependence of the droplet sizes on grid resolution. For all cases, a bimodal droplet distribution is observed, with a clear segregation between one group of droplets that represent "physical" droplets after breakup and the artificial/satellite droplets. For the higher refinement levels the number density of smaller diameters increases. Nonetheless, as demonstrated by the distribution functions shown in Fig. 6, that show the distribution of mass-weighted droplet diameters, these droplets account for a very small fraction of the spray mass or volume.

It is also noted that the reference droplet size D_{ref} (Eq.11) offers a good estimation for the minimum droplet size (see horizontal dashed line in Fig. 4). For Case B the size of the main droplet group seems to converge towards this value. For Case A, the resulting droplets are – on average – half the size of D_{ref}, still indicating that D_{ref} may provide a suitable estimate but cannot be taken as a precise measure for the droplet distribution after breakup.

The results shown in Fig. 7 provide and indication of the importance of lamella breakup for the final droplet distribution of the entire spray. The spray volume fraction, Q_{Vol}, is calculated relative to a reference control volume that approximates the liquid initially in the domain, V_{dom}. Then, using the total (unfiltered) volume of liquid given by Eq. 12, Q_{Vol}

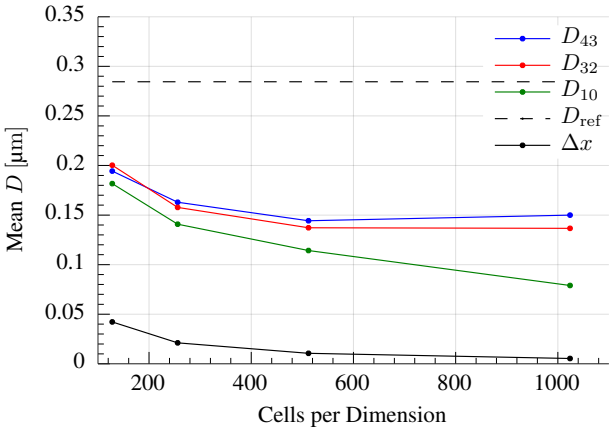

(a) Case A $T_\infty = 120\,\text{K}$

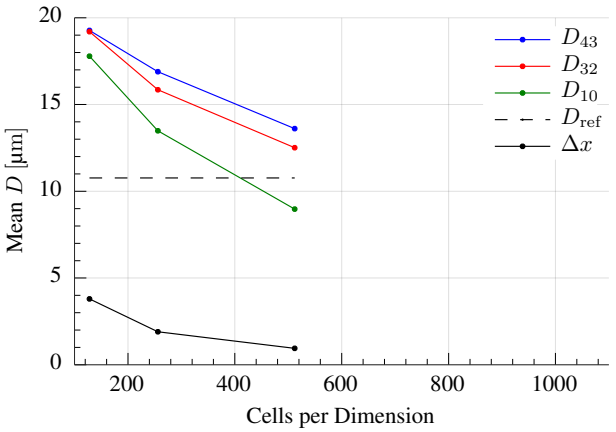

(b) Case B $T_\infty = 80\,\text{K}$

Figure 4: Dependency of the D_{10} (arithmetic), D_{32} (Sauter) and D_{43} (De Brouckere) mean diameters with the mesh refinement for both cases studied and comparison with the cell size Δx and estimated droplet size D_{ref} (Eq.11)

is given by:

$$Q_{\text{Vol}} = \frac{\sum_{i=1}^{N_i} V_i}{V_{\text{dom}}}, \tag{20}$$

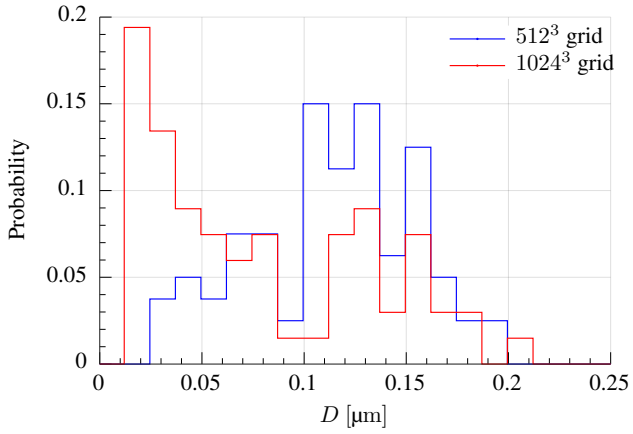

(a) Case A $T_\infty = 120\,\mathrm{K}$

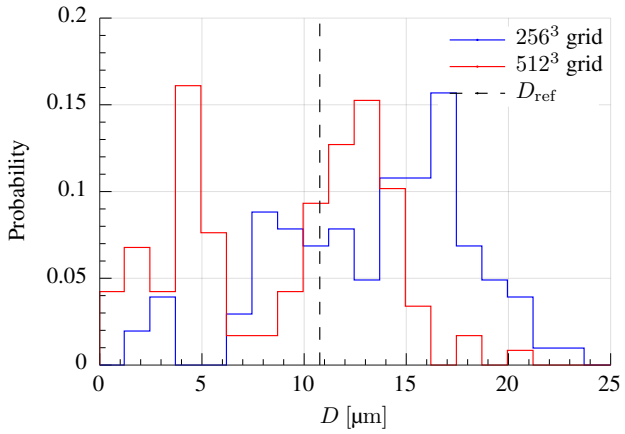

(b) Case B $T_\infty = 80\,\mathrm{K}$

Figure 5: Discrete probability density functions (PDF) of the equivalent droplet diameter D_i (filtered) for cases A and B at the two highest levels of mesh refinement for each case

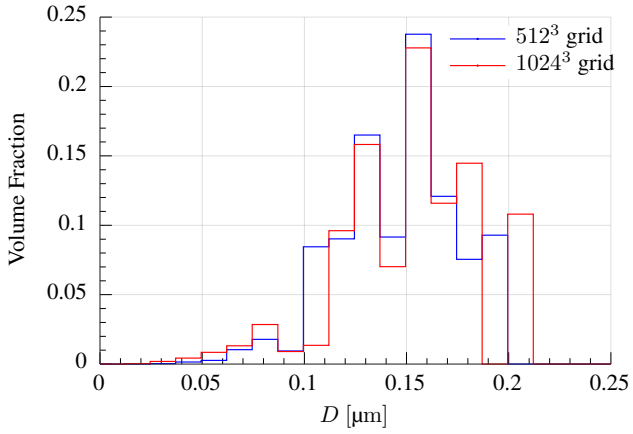

(a) Case A $T_\infty = 120\,\mathrm{K}$

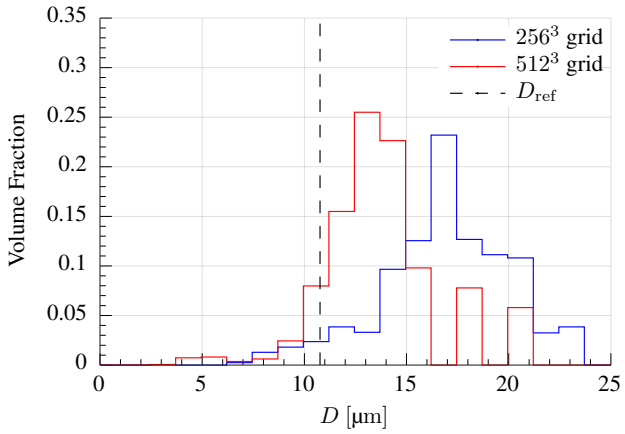

(b) Case B $T_\infty = 80\,\mathrm{K}$

Figure 6: Discrete volume fraction distribution function of the equivalent droplet diameter D_i (filtered) for cases A and B at the two highest levels of mesh refinement for each case

It is shown that the volume associated with lamella breakup is much larger for Case B, which has a larger Weber number ($\mathrm{We}_b = 80$), and is highly dependent on the grid. This may indicated the need for 1024^3 grid points for case B despite the relatively small variation (25%) of D_{43} shown in Fig. 4b. For case Case A, not only the variation of D_{43} shown in Fig. 4a is extremely small, but the relative volume consumed by the lamella, shown in Fig. 7, is also very small.

6 Conclusions

A mesh refinement study corroborates existing studies inasmuch the minimum droplet size decreases with increasing resolution and seems to be mesh dependent. However, the mass weighted droplet diameter tends to converge towards a given size that can be estimated by analysis of surface and kinetic energy acting on the bubble walls.

The exact average droplet diameter may deviate from this estimate by a factor of 2, however, an increase in resolution also demonstrates that the overall liquid mass associated with lamellae breakup approaches single digit percentage values and the highest resolution may not be needed for adequate approximation of the entire spray breakup process.

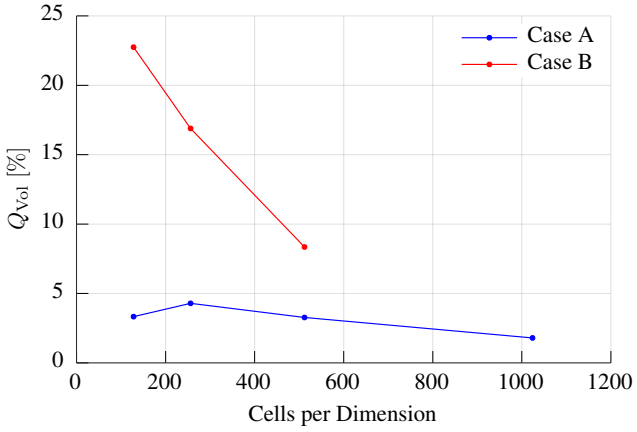

Figure 7: Spray volume fraction relative to the initial volume of liquid.

Acknowledgments

This work is part of the HAoS-ITN project and has received funding from the European Union's Horizon 2020 research and innovation programme under the Marie Skłodowska-Curie grant agreement No 675676 (DL). We also acknowledge funding by DFG through the Collaborative Research Center SFB-TRR75 (JR, AK, BW) and by the UK's Engineering and Physical Science Research Council support through the grant EP/P012744/1 (KV).

References

R. Bardia and M. F. Trujillo. Assessing the physical validity of highly-resolved simulation benchmark tests for flows undergoing phase change. *International Journal of Multiphase Flow*, 112, 12 2018. doi: 10.1016/j.ijmultiphaseflow.2018.11.018.

I. H. Bell, J. Wronski, S. Quoilin, and V. Lemort. Pure and pseudo-pure fluid thermophysical property evaluation and the open-source thermophysical property library coolprop. In *Industrial & Engineering Chemistry Research*, volume 53, pages 2498–2508. 2014. doi: 10.1021/ie4033999.

X. Chen, D. Ma, V. Yang, and S. Popinet. High-fidelity simulations of impinging jet atomization. *Atomization and Sprays*, 23(12):1079–1101, 2013. ISSN 1044-5110.

O. Desjardins, V. Moureau, and H. Pitsch. An accurate conservative level set/ghost fluid method for simulating turbulent atomization. *Journal of Computational Physics*, 227:8395–8416, 09 2008. doi: 10.1016/j.jcp.2008.05.027.

K. Eisenschmidt, M. Ertl, H. Gomaa, C. Kieffer-Roth, C. Meister, P. Rauschenberger, M. Reitzle, K. Schlottke, and B. Weigand. Direct numerical simulations for multiphase flows: An overview of the multiphase code FS3D. *Journal of Applied Mathematics and Computation*, 272(2):508–517, 1 2016.

M. Ertl, J. Reutzsch, A. Nägel, G. Wittum, and B. Weigand. Towards the implementation of a new multigrid solver in the dns code fs3d for simulations of shear-thinning jet break-up at higher reynolds numbers. In *High Performance Computing in Science and Engineering ' 17*, pages 269–287. Springer International Publishing, 2018. ISBN 978-3-319-68394-2.

M. Gorokhovski and M. Herrmann. Modeling primary atomization. *Annual Review of Fluid Mechanics*, 40(1):343–366, 2008. doi: 10.1146/annurev.fluid.40.111406.102200.

J. O. Hinze. Fundamentals of the hydrodynamic mechanism of splitting in dispersion processes. *AIChE Journal*, 1(3): 289–295, 1955. doi: 10.1002/aic.690010303.

C. W. Hirt and B. D. Nichols. Volume of fluid (vof) method for the dynamics of free boundaries. *Journal of computational physics*, 39(1):201–225, 1981.

E. Hurlbert, J. Applewhite, T. Nguyen, B. Reed, Z. Baojiong, and W. Yue. Nontoxic Orbital Maneuvering and Reaction Control Systems for Reusable Spacecraft. *Journal of Propulsion and Power*, 14(5):676–687, 1998. ISSN 0748-4658. doi: https://doi.org/10.2514/2.5330.

B. Lafaurie, C. Nardone, R. Scardovelli, S. Zaleski, and G. Zanetti. Modelling merging and fragmentation in multiphase flows with surfer. *Journal of Computational Physics*, 113(1):134 – 147, 1994. ISSN 0021-9991.

R. Lebas, T. Menard, P. Beau, A. Berlemont, and F. Demoulin. Numerical simulation of primary break-up and atomization: Dns and modelling study. *International Journal of Multiphase Flow*, 35(3):247 – 260, 2009. ISSN 0301-9322. doi: https://doi.org/10.1016/j.ijmultiphaseflow.2008.11.005.

H. S. Lee and H. Merte. Spherical vapor bubble growth in uniformly superheated liquids. *International Journal of Heat and Mass Transfer*, 39(12):2427–2447, 1996.

M. Liu and D. Bothe. Numerical study of head-on droplet collisions at high weber numbers. *Journal of Fluid Mechanics*, 789:785–805, 02 2016.

D. Loureiro, J. Reutzsch, D. Dietzel, A. Kronenburg, B. Weigand, and K. Vogiatzaki. DNS of multiple bubble growth and droplet formation in superheated liquids. In *14th International Conference on Liquid Atomization and Spray Systems ,Chicago, IL, USA*, July 2018.

C. Manfletti. Laser Ignition of an Experimental Cryogenic Reaction and Control Thruster: Pre-Ignition Conditions. *Journal of Propulsion and Power*, 30(4):925–933, 2014.

A. Prosperetti. Vapor bubbles. *Annual review of fluid mechanics*, 49, 2017.

M. Razzaghi. Droplet size estimation of two-phase flashing jets. *Nuclear Engineering and Design*, 114(1):115 – 124, 1989. ISSN 0029-5493. doi: https://doi.org/10.1016/0029-5493(89)90130-1.

W. J. Rider and D. B. Kothe. Reconstructing volume tracking. *Journal of computational physics*, 141(2):112–152, 1998.

M. Rieber. *Numerische Modellierung der Dynamik freier Grenzflachen in Zweiphasenstromungen*. PhD thesis, Universität Stuttgart, 2004.

E. Ruckenstein and R. K. Jain. Spontaneous rupture of thin liquid films. *Journal of the Chemical Society, Faraday Transactions 2: Molecular and Chemical Physics*, 70:132–147, 1974.

J. Schlottke and B. Weigand. Direct numerical simulation of evaporating droplets. *Journal of Computational Physics*, 227:5215–5237, 2008.

L. Scriven. On the dynamics of phase growth. *Chemical Engineering Science*, 10(1):1 – 13, 1959. ISSN 0009-2509. doi: https://doi.org/10.1016/0009-2509(59)80019-1.

E. Sher and C. Elata. Spray formation from pressure cans by flashing. *Industrial & Engineering Chemistry Process Design and Development*, 16(2):237–242, 1977.

E. Sher, T. Bar-Kohany, and A. Rashkovan. Flash-boiling atomization. *Progress in Energy and Combustion Science*, 34:417–439, 08 2008.

J. Shinjo and A. Umemura. Simulation of liquid jet primary breakup: Dynamics of ligament and droplet formation. *International Journal of Multiphase Flow*, 36(7):513–532, 2010.

Y. Zeng and C.-F. F. Lee. An atomization model for flash boiling sprays. *Combustion Science and Technology*, 169(1): 45–67, 2001.

C. Zhu, M. Ertl, and B. Weigand. Numerical investigation on the primary breakup of an inelastic non-newtonian liquid jet with inflow turbulence. *Physics of Fluids*, 25(8):083102, 2013. doi: 10.1063/1.4818305.